Radiology: Imaging Cancer

ORIGINAL RESEARCH

Ex Vivo MR Histology and Cytometric Feature Mapping Connect Three-dimensional in Vivo MR Images to Two-dimensional Histopathologic Images of Murine Sarcomas

Stephanie J. Blocker, PhD • James Cook, BS • Yvonne M. Mowery, MD, PhD • Jeffrey I. Everitt, DVM • Yi Qi, MD • Kathryn J. Hornburg, PhD • Gary P. Cofer, MS • Fernando Zapata, BS • Alex M. Bassil, BA • Cristian T. Badea, PhD • David G. Kirsch, MD, PhD • G. Allan Johnson, PhD

From the Departments of Radiology (S.J.B., J.C., Y.Q., K.H., G.P.C., F.Z., C.T.B., G.A.J.), Radiation Oncology (Y.M.M., A.M.B., D.G.K.), and Pathology (J.I.E.), Duke University Medical Center, Center for In Vivo Microscopy, Bryan Research Building, 311 Research Dr, Durham, NC 27710. Received July 16, 2020; revision requested September 9; revision received March 1, 2021; accepted March 11. **Address correspondence to** S.J.B. (e-mail: *stephanie.blocker@duke.edu*).

Supported by the National Cancer Institute (grants NCI U24 CA220245 and NCI R35CA197616). D.G.K. supported by grant R35CA197616 from the National Cancer Institute.

Conflicts of interest are listed at the end of this article.

Radiology: Imaging Cancer 2021; 3(3):e200103 • https://doi.org/10.1148/rycan.2021200103 • Content codes: MR OI

Purpose: To establish a platform for quantitative tissue-based interpretation of cytoarchitecture features from tumor MRI measurements.

Materials and Methods: In a pilot preclinical study, multicontrast in vivo MRI of murine soft-tissue sarcomas in 10 mice, followed by ex vivo MRI of fixed tissues (termed *MR histology*), was performed. Paraffin-embedded limb cross-sections were stained with hematoxylin-eosin, digitized, and registered with MRI. Registration was assessed by using binarized tumor maps and Dice similarity coefficients (DSCs). Quantitative cytometric feature maps from histologic slides were derived by using nuclear segmentation and compared with registered MRI, including apparent diffusion coefficients and transverse relaxation times as affected by magnetic field heterogeneity (T2* maps). Cytometric features were compared with each MR image individually by using simple linear regression analysis to identify the features of interest, and the goodness of fit was assessed on the basis of R^2 values.

Results: Registration of MR images to histopathologic slide images resulted in mean DSCs of 0.912 for ex vivo MR histology and 0.881 for in vivo MRI. Triplicate repeats showed high registration repeatability (mean DSC, >0.9). Whole-slide nuclear segmentations were automated to detect nuclei on histopathologic slides (DSC = 0.8), and feature maps were generated for correlative analysis with MR images. Notable trends were observed between cell density and in vivo apparent diffusion coefficients (best line fit: $R^2 = 0.96$, $P < .001$). Multiple cytoarchitectural features exhibited linear relationships with in vivo T2* maps, including nuclear circularity (best line fit: $R^2 = 0.99$, $P < .001$) and variance in nuclear circularity (best line fit: $R^2 = 0.98$, $P < .001$).

Conclusion: An infrastructure for registering and quantitatively comparing in vivo tumor MRI with traditional histologic analysis was successfully implemented in a preclinical pilot study of soft-tissue sarcomas.

Supplemental material is available for this article.

MRI has earned a permanent place in the oncologist's toolkit, and interest in quantitative MRI assessment of tumor properties is steadily growing (1–5). Imaging-derived tissue metrics such as the apparent diffusion coefficient (ADC) at diffusion-weighted MRI have shown promise for characterizing tumors (6–8). Despite early enthusiasm, however, attempts to use ADC values to distinguish tumor subclasses or states of progression have yielded inconsistent findings (9–11). Comprehensive interpretation of quantitative MRI findings requires insight into the relationship between tissue characteristics and MRI signals. Deciphering this relationship in tumors is complicated by heterogeneity, whereby diverse cellular environments may be within a region of interest. Experiments comparing tumor histologic characteristics and MRI findings are frequently limited to regional measurements (12–15), which may not accurately describe subtumoral heterogeneity. Since tissue histologic analysis is the reference standard for classifying tumor tissues, advanced MRI findings interpretation requires a means of directly comparing histologic tissue sample findings with multicontrast MR image features.

The gap between histologic and MRI data stems from fundamental challenges in image registration, including differences in image spatial resolution, image signal type, and tissue intactness (16–19). While registering histopathologic findings to MR image features is difficult, the benefits of doing so include improved tumor delineation in radiologic imaging (20,21), identification of unseen tumor foci (22), and improved understanding of how to properly stage tumors on the basis of radiologic signatures (23–25). With preclinical studies, imaging technologies with spatial resolution higher than what is clinically viable can be used and whole-mount tissue specimens of a variety of tumor types can be obtained. In addition, these studies can be performed in elegant, genetically engineered models of disease. While the challenges of image registration persist, the

Abbreviations

ADC = apparent diffusion coefficient, DSC = Dice similarity coefficient, H-E = hematoxylin-eosin, MRH = MR histology, 3D = three dimensional, 2D = two dimensional

Summary

A preclinical multiscale image registration platform facilitated reliable correlative studies of whole-slide cytometric feature maps and MR images to characterize how cytoarchitecture influences MRI measurements.

Key Points

- With use of high-spatial-resolution ex vivo MR histology of fixed tissues as a conduit, three-dimensional MR images of murine sarcomas were registered to two-dimensional histologic images with high repeatability (Dice similarity coefficient [DSC], >0.9).
- Nuclear segmentation was automated over entire tumor cross-sections (>600 000 nuclei per slide), with improved detection of complex nuclear shapes (DSC = 0.8), compared with the detection at hematoxylin watershed segmentation (DSC < 0.6). From these segmentations, quantitative cytometric feature maps of 48 features were generated and compared with registered MR images.
- Multiple sarcoma samples demonstrated linear relationships between cytometric features and MRI signals, including cell detection counts derived by using apparent diffusion coefficient values and nuclear circularity derived by using T2*.

Keywords

MRI, Pathology, Animal Studies, Tissue Characterization

limited examples of preclinical cancer studies in which imaging and histopathologic analysis are combined are promising. Examples include MRI-based vascularity evaluation in a subcutaneous neuroendocrine tumor model (26), preliminary MR image feature identification in a patient-derived glioblastoma model (27), MRI-based assessment of extratumoral glioblastoma cell infiltration in orthotopic xenografts (28), and whole-tumor assessment of heterogeneous angiogenesis in breast tumor xenografts with multimodality imaging (2). By establishing a means of reliable registration and analysis, preclinical studies can be used to decipher MRI tumor signal on the basis of tissue histologic characteristics. The specific objectives of this study were twofold: *(a)* to develop a method to register and align MR images to histopathologic slide images and *(b)* to perform correlative analysis of MRI and histopathologic features. These applications can be used to better understand how tumor architecture influences MRI signals.

Materials and Methods

Study Design

We developed protocols for multiparametric image registration spanning from in vivo three-dimensional (3D) MR images to two-dimensional (2D) optical histopathologic sections. To meet the challenge of disparate image resolutions, we bridged MRI and histopathologic data with high-spatial-resolution ex vivo MRI of resected tissues; this procedure is termed *MR histology* (MRH) (29,30). To address the difference in signal type, we developed high-throughput protocols for quantifying the physical properties of hematoxylin-eosin (H-E)–stained histopathologic samples. Together, these methods facilitated subtumoral correlative histopathologic and MRI experiments. Furthermore, our constructed environment, Image Space, enabled us to execute these correlative studies with use of very large preclinical data sets of soft-tissue sarcoma. The developed methodologies enabled the identification of numerous correlations between H-E–derived cytometric property maps and registered MR images.

Animal Studies

Pilot tumor studies were performed by using two genetically engineered murine models of soft-tissue sarcoma of the hind limb of 10 mice. These tumors resemble undifferentiated pleomorphic sarcomas in terms of their histologic features and gene expression profile (31). The sarcoma models were studied as part of a U24 co-clinical trial (U24 CA220245) of imaging biomarkers in sarcomas treated with immune checkpoint blockade, radiation therapy, and surgery. The tumor induction process is described in Appendix E1 (supplement). All animal studies were reviewed and approved by the Institutional Animal Care and Use Committee at Duke University.

MRI Parameters

Table 1 describes the general MRI parameters for in vivo and ex vivo imaging at 7 T. MRI was performed in vivo in live animals, and ex vivo MRI of fixed tissue, which included sequences for anatomic landmark identification and derived maps (Fig 1), was performed. In vivo MRI experiments were performed by using a 7-T Biospec small-animal MRI scanner (Bruker). The animals were imaged in a lateral recumbent position in a custom 3D-printed bed heated with integrated warm water circulation. Anesthesia was induced with atomized isoflurane at 2.5% and maintained at 1%–2% with an integrated nose cone. Their vital signs were monitored for the duration of imaging. After the animals were sedated, a four-element mouse brain coil was positioned over the secured tumor-bearing limb. The bed and coil platform were centered in a 72-mm diameter, actively decoupled linear volume coil for transmission. Image acquisition was performed by using a ParaVision 360, version 6.0.1 (Bruker), MR unit. The images were stored in Digital Imaging and Communications in Medicine format. In vivo MRI included anatomic T1-weighted fast low-angle shot (33,34), T2-weighted turbo rapid acquisition with relaxation enhancement (35,36), multigradient-recalled-echo, and spiral-trajectory diffusion-weighted sequences. The total acquisition time was less than 90 minutes per animal.

Once the live-animal imaging examinations were complete, the animals were euthanized in accordance with Instructional Animal Care and Use Committee guidelines, and the tumor-harboring limbs were removed. The resected legs were immersed in 10% formalin doped with 1% gadolinium (Bracco Diagnostics, Monroe, NJ) to reduce the spin lattice relaxation time (T1) of the tissue. The specimens were fixed in formalin for 72 hours, during which time the fixative was changed twice. The specimens were then rehydrated with saline containing 1% gadolinium for 1 week. Imaging of the specimens was performed by using a 7-T horizontal

Table 1: Basic MRI Parameters for in Vivo and ex Vivo MRI Acquisition

Sequence	Value(s)	Acquisition Time
In vivo imaging		
T1-weighted FLASH sequence	…	10 min
TE (msec)	4.5	NA
TR (msec)	925	NA
Flip angle (°)	30	NA
No. of excitations	three	NA
T2 TurboRARE sequence	…	15 min
TE (msec)	45	NA
TR (msec)	8600	NA
RARE	8	NA
No. of excitations	Three	NA
Spiral DWI sequence	…	20 min
b Values (sec/mm^2)	0, 100, 300, 500	NA
Interleaves	40	NA
No. of excitations	Two	NA
MGRE sequence	…	16 min
TE (msec)	4, 19, 34, 49	NA
No. of excitations	Three	NA
Ex vivo imaging		
Spiral DWI sequence	…	2 h
b Values (sec/mm^2)	0, 500, 1000, 1500, 2000	NA
Compression factor	5	NA
MGRE sequence	…	2 h
TE (msec)	3.2, 9.3, 15.5, 21.6	NA
Compression factor	8	NA

Note.—For in vivo T1-weighted fast low-angle shot (FLASH) and T2-weighted turbo rapid acquisition with relaxation enhancement (TurboRARE) MRI, 0.1 × 0.1 × 0.3 voxels were used. For in vivo spiral diffusion-weighted (DWI) and multigradient-recalled echo (MGRE) MRI, 0.1 × 0.1 × 0.6 voxels were used. For ex vivo spiral DWI and MGRE MRI, 0.5 × 0.5 × 0.5 voxels were used. NA = not applicable, TE = echo time, TR = repetition time.

bore magnet with high-performance resonance research gradient coils (650 mT/m peak) controlled by using an Agilent Direct Drive console (Agilent Technologies). Tissues were immersed in fomblin (Sigma-Aldrich) to minimize susceptibility effects at the sample surface.

A single-sheet solenoid resonator was constructed in-house to provide high sensitivity. All imaging examinations were performed by using an integrated compressed sensing acquisition–reconstruction pipeline (38). The 3D isotropic multigradient-recalled-echo and Stejskal-Tanner diffusion-weighted MRI sequences were used with 2D phase encoding. The phase-encoding directions were sparsely sampled by using a view table defined in MATLAB code (Mathworks) by using probabilistic methods (39). Data from the Agilent scanner were streamed during acquisition to the high-performance cluster. A Fourier transform was executed along the fully sampled readout axis, producing sparsely sampled 2D arrays that were parsed into multiple jobs in the cluster for iterative reconstruction.

Reconstruction during acquisition, as well as splitting of reconstruction into parallel jobs on the cluster, mitigated the time cost of compressed sensing. For example, reconstruction of the four-dimensional diffusion arrays typically was completed within 1 hour after acquisition completion. An acceleration factor of 8 was used, resulting in a spatial resolution of 50 μm^3, with acquisition times of approximately 4 hours. Sequence information is provided in Table 1. A typical four-dimensional diffusion-weighted imaging data set, including four volumes at an array size of 360 × 360 × 760, yields approximately 466 MB of raw data and 2.2 GB of image data. Each ex vivo MRH data set generated approximately 6.7 GB of raw and reconstructed data per tissue sample.

Histologic Specimen Preparation

Specimens with intact bone were decalcified in 14% ethylenediaminetetraacetic acid for 14 days and then stored in 70% ethanol prior to paraffin embedment. Tissues from the section of the leg that contained the tibia and fibula were trimmed into three sections: top (superior), middle, and bottom (inferior). Slices were 6 μm in thickness and were taken from each section and stained with H-E. The stained slides were digitized (spatial resolution, 0.2523 μm) on an Aperio AT2 whole-slide scanner (Leica Biosystems, Buffalo Grove, Ill) and exported in SVS format. Original histologic images (200–850 MB per slide) were analyzed without downsampling by using QuPath (*https://qupath.github.io/*) (40).

Infrastructure for Data Handling

We constructed an infrastructure for reconstructing, cataloging, and analyzing libraries that included in vivo MRI, ex vivo MRH images (500–900 MB per volume), and optical images (≤1.5 GB per slide). We called this infrastructure Image Space; and it is further described in Figure E1 (supplement). In addition, a detailed description of the Image Space environment for large image data is provided in Appendix E2 (supplement). The Image Space facilitates parallel reconstruction of multicontrast ex vivo MRH data sets, enables efficient assembly of data from multiple sources, and improves processing times during large-scale data analyses.

Multimodal Image Registration

Image registration was performed by using 3D Slicer (41) open-source platform software *(https://www.slicer.org)* (Fig E2 [supplement]). The two phases of registration were as follows: *(a)* in vivo MR

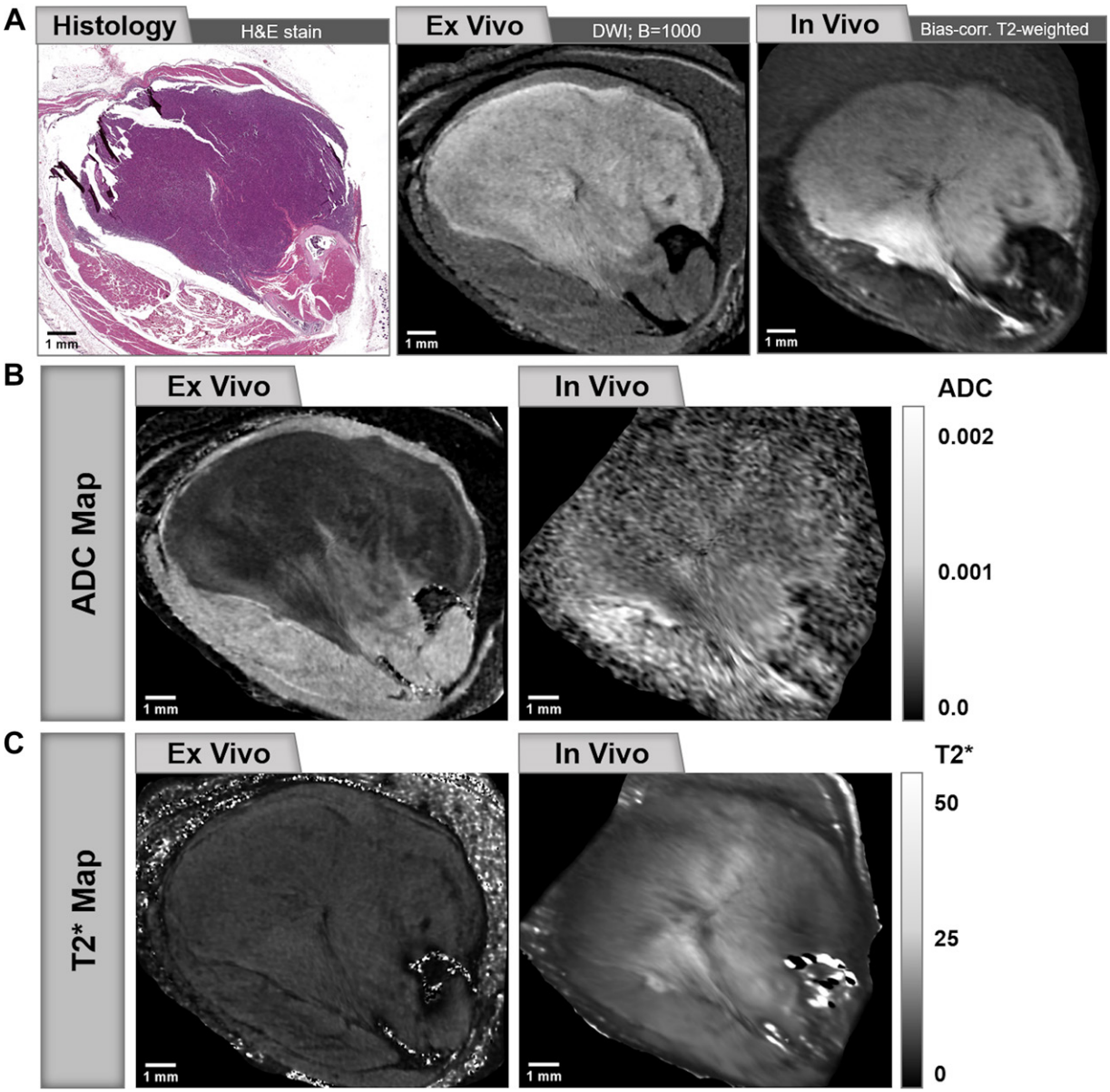

Figure 1: High-resolution ex vivo MRH and in vivo MRI sequences for imaging soft-tissue sarcoma in a murine model. *A,* Multiplatform, multiresolution images of hind limb soft-tissue sarcoma were obtained: a two-dimensional (2D) histologic MR image of a hematoxylin-eosin (H&E)–stained cross-section of a tumor (left), an ex vivo MRH diffusion-weighted image (DWI) at a *b* value of 1000 sec/mm^2 and 5-μm isotropic resolution (middle), and an in vivo bias-corrected T2-weighted MR image (right). *B, C,* Also shown are examples of in vivo and ex vivo derived maps of, *B,* apparent diffusion coefficient (ADC) and, *C,* T2* images.

images to ex vivo MRH images and *(b)* ex vivo MRH images to histopathologic images. The ex vivo MRH images were ultimately used as a conduit for aligning in vivo MR images and histopathologic slide images, accounting for shrinkage and distortions during the fixation process. At each phase there were three steps of alignment. The steps for in vivo MR image registration to ex vivo MRH images are illustrated in Figure E3 (supplement) and described in Appendix E3 (supplement).

To facilitate optimal alignment of ex vivo MRH slide images to histopathologic slide images, a hybrid MRH image was created by multiplying the sum of all multigradient-recalled echoes and the diffusion-weighted image at a *b* value of 1000 sec/mm^2. The resulting image included both the structural detail of the multigradient-recalled echo sum image (bone, cartilage, and nerve detail) and the soft-tissue contrast of the diffusion-weighted image (Fig E4 [supplement]). The steps for ex vivo MRH image registration to the histopathologic slide images are illustrated in Figure E5 (supplement) and described in Appendix E4 (supplement). Each ex vivo MRH image was processed through the same series of transformations. Finally, the in vivo MR images that had been aligned to the ex vivo MRH images also were passed through the 3D-to-2D transformations. The result was a collection of in vivo and ex vivo MR images aligned to the 2D histopathologic slides.

Quantitation of Registration Success and Repeatability

To assess the success of image registration, binary masks delineating tumor tissues were defined on native images, including in vivo MRI, ex vivo MRH, and digitized H-E histopathologic

images. Three-dimensional binary masks were generated on MR images by using semiautomated segmentation techniques, which were described previously (42). Three-dimensional tumor masks were registered to the histopathologic images by using the defined transformation matrices described above. The resulting images were 2D binary masks of tumor MRI regions. Two-dimensional tumor masks were generated from the H-E slides by using thresholding regions of hematoxylin signal above 0.25 in ImageJ (*https://imagej.net*). Both in vivo and ex vivo mask results were compared with histopathologic analysis–derived masks, and a Dice similarity coefficient (DSC) was generated for each registration (46,47). A minimal DSC of 0.8 was required for success, with a DSC of less than 0.8 considered unsatisfactory.

To quantitate the effect of the manual steps on registration, repeatability was assessed in three samples (slides 2, 8, and 12) by performing full image registration in triplicate. Three histologic slides (from different animals) in which the full tumor boundary was intact and free from tearing artifacts were selected. This reduced the effect of lost tissue on tumor mask comparison. Binary tumor masks were run through each registration attempt independently, and the results of the three repeats from each sample were compared. Jaccard similarity coefficient and DSC comparisons were used to assess repeat registration.

Automated Nuclear Segmentation

To compare MRI signal with histologic properties, reliable nuclear segmentation from H-E images was performed. Noting the shortcomings of single-step watershed-based detection techniques in heterogeneous tissues (49,50), several multistep processes were explored. A pathologist (J.I.E.) evaluated segmentation protocols against manual segmentations in 15 tiles from three tissue specimens. Automated segmentation results were assessed for true-positive identification of nuclei by comparing DSCs (46,47,49).

Segmentation consisted of a multistep approach involving the use of a combination of the public domain image analysis platforms QuPath, ImageJ (50), and FIJI *(https://imagej.net/Fiji)* (51). The tested protocols were distinguished by differences in the type, order, and magnitude of adjustments made to the image such as thresholding and Fourier transformations. The steps of the selected nuclear segmentation protocol are briefly described in Appendix E5 (supplement) (52). Segmentation was performed on all samples without the need for sample-specific parameter changes. The process was automated with a code written as a plugin for FIJI, which enabled bulk processing of all tiles associated with a sample.

Cytometric Property Map Generation

Once whole-slide nuclei were segmented, measurements of each nucleus were made within QuPath by using the fully sampled H-E image. Measurements included shape characteristics, intranuclear hematoxylin Haralick texture features (53), and Delaunay triangulation measurements (54). A total of 48 features were measured for each nucleus (600 000 to 2 million nuclei per sample) in QuPath. Select cytometric features are defined in Figure E6 (supplement). From these data, quantitative maps of cellular metrics were generated with a code developed in-house by using MATLAB, described in Appendix E6 (supplement) and demonstrated in Figure E7 (supplement).

ADC and T2* Image Analysis

On the original MR images (ie, in vivo MRI and ex vivo MRH images), regions of interest were segmented in 3D by using semiautomated techniques described previously (42). We measured the span of ADC and T2* across all in vivo and ex vivo images (Fig 2, first column). Histograms of ADC and T2* signal in tumor were measured in all samples and normalized to the peak value to correct for tissue size. Boundaries were defined at ± 2 standard deviations of the signal Gaussian mean (Fig 2, second column). This curve was used to discretize the MRI signal into six bins of approximately the same area under the curve (55,56). A macro was developed in ImageJ to bin the ADC and T2* maps for each sample based on thresholds of those signals, respectively. The resulting six regions defined the sampling of registered cytometric feature maps. When applied to a given sample, the macro automatically discretizes the MRI signal into the appropriate bins to create regions of interest (Fig 2, fourth column). The tool then correlates the MRI signal in the bin to all cytometric maps for that sample and generates measurement tables, including mean and standard deviation values per region of interest. Regions of interest that represented less than 5% of the total measured pixels were excluded to reduce registration confounds. The plugin performs MRI segmentation and region-of-interest measurements for all feature maps for a sample in approximately 1 minute per MR image. Binning and generation of the tables with this tool were completed in approximately 10 minutes per sample in the Image Space environment.

Tables were imported into Prism (version 8.00 for Windows; GraphPad Software, San Diego, Calif) for plotting and linear regression analysis. Mean cytometric property values were plotted against the mean MRI measurement within the corresponding region. For preliminary studies, cytometric properties of interest were those that demonstrated linear relationships with an MRI metric (ADC or T2*) with a measurable nonzero slope in multiple samples. Examples of best linear fits are reported.

Statistical Analysis

Statistical analyses were performed by using Prism. For individual samples, each cytometric property (mean ± standard deviation) was compared with the ADC or T2* maps. Simple linear regression analysis was used to identify correlations between individual cytometric features and ADC or T2* values. In this analysis, the MRI signal bins ($n = 6$) defined sampling. Goodness of fit was assessed on the basis of the R^2 value of the regression on a per-sample basis. Features of interest were identified as regressions with slopes that statistically deviated from zero ($P < .05$) in multiple samples.

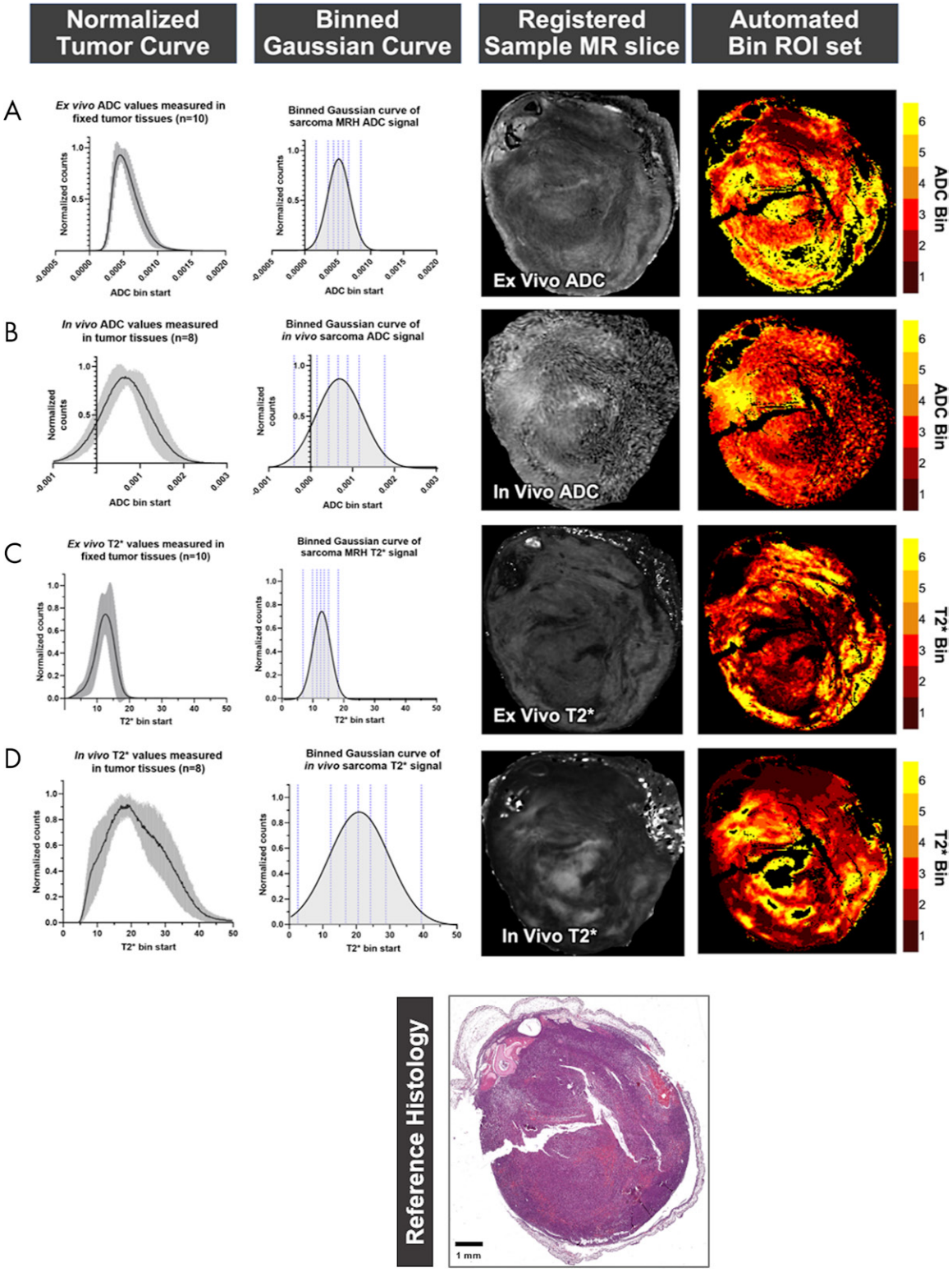

Figure 2: Automated region of interest (ROI) generation based on MRI signal binning. Segmentations of entire tumor volumes were measured in all samples and used to generate normalized tumor curves for, *A*, ex vivo apparent diffusion coefficient (ADC), *B*, in vivo ADC, *C*, ex vivo T2*, and, *D*, in vivo T2*. The first column depicts the group measurements of tumor in all samples. The second column depicts the Gaussian curves of these data, which were divided into bins (denoted by blue dashed lines) of approximately equal area under the curve. Examples are shown of automated ROI generation (right column) for a sample, determined by the signal bins. Black regions on the bin map (fourth column) represent areas in which no tumor tissue was present on the histopathologic slide (eg, tears in the tissue), and thus have been voided. The histological tissue slide, to which the MRI has been registered, is also provided for reference. MRH = MR histology image analysis.

Results

Multiparametric Image Registration Pipeline Demonstrates Reliable Repeatability

In the 10 mice in the study, a total of 16 specimens from nine tumors were deemed suitable for image analysis. The distribution was as follows: One tumor produced three usable slides; five tumors produced two usable slides; three tumors produced one usable slide; and one tumor produced no usable slides owing to tissue-mounting issues. Per sample, image registration required approximately 1–2 hours of experienced user participation, plus 2 hours of unsupervised processing time. Use of the Image Space platform improved registration in two ways: *(a)* Fully sampled data sets from multiple sources could be efficiently moved for side-by-side comparison without loss of information and/or detail, and *(b)* calculation of 3D transformation matrices for very large data sets was not subject to memory restraints when performed on the grid servers.

To ensure the reliability of registration, a series of comparisons were made between the transformed MRI tumor masks and histopathologic tumor masks. For each slide, in vivo– and ex vivo–derived masks were compared with H-E masks and assigned a DSC (Fig 3, *A*). One sample did not meet the minimal DSC criteria, demonstrating an ex vivo DSC of 0.408 and an in vivo DSC of 0.290. For the remaining samples, the mean ex vivo DSC was 0.912, and the mean in vivo DSC was 0.881 for alignment to the histopathologic slide images. Repeatability of registration methods was assessed on three representative slides (Fig 3, *B*). For each slide, triplicate registration repeats resulted in a mean DSC of greater than 0.9 both in vivo and ex vivo, and Jaccard similarity coefficients of greater than 85% ex vivo and greater than 84% in vivo, indicating that registration was reliably repeatable. Repeatability results are reported in Table 2. Together, these results indicate that the registration process of aligning in vivo MR images with histopathologic slide images resulted in accurate alignment.

MRH and Cytometric Feature Mapping Facilitates Identification of Preliminary Correlates between MRI Signal and Histologic Features

Next, cytometric feature maps of entire histologic slides were compared with histologically aligned MR images. Nuclear segmentation was performed by using FFT3 (Appendix E7 [supplement]), which improved nuclear segmentation (DSC = 0.8), as compared with the segmentation achieved by using hematoxylin optical-density watershed techniques (DSC $<$ 0.6) (Fig 4, *A, B*). Cytometric features were extracted from nuclear masks by using QuPath (Fig 4, *C*). Simple linear regressions were generated in individual tissue samples to identify cytometric properties of interest. Detection counts (cell density) and Delaunay ratios demonstrated linear relationships with ADCs in multiple samples (Fig 5). Detection counts measured in individual samples showed linear correlations with both ex vivo ADC (best line fit: R^2 = 0.95, $P < .001$) and in vivo ADC (best line fit: R^2 = 0.96, $P < .001$). Delaunay ratios measured in samples also demonstrated linear relationships with ex vivo ADC (best line fit: R^2 = 0.98, $P < .001$) and in vivo ADC (best line fit: R^2 = 0.97, $P < .001$).

A distinct collection of cytometric features, including nuclear circularity and variance in nuclear circularity, showed a linear relationship with in vivo T2* (Fig 6) in multiple tissue samples. Nuclear circularity at histopathologic analysis consistently showed a correlation with in vivo T2* (best line fit: R^2 = 0.99, $P < .001$) but not ex vivo T2* (best line fit: R^2 = 0.42, P = .16). Similarly, the variance in nuclear circularity showed linear relationships with in vivo T2*, but not ex vivo T2* (best line fit: R^2 = 0.32, P = .24), in multiple samples (best line fit: R^2 = 0.98, $P < .001$).

Discussion

A major challenge in using advanced MRI for clinical cancer management is the disconnect between imaging and histopathologic assessment. Clinically, histopathologic reports remain a cornerstone of tumor identification and staging (57–59). Efforts to relate tumor MRI findings to histopathologic analysis features are challenged by interdisciplinary differences between the fields and the data they handle (16). To meet these challenges, we constructed an environment that is capable of handling very large data sets for statistically viable studies of tumor imaging features. By using this platform, we have demonstrated the use of protocols for registering multimodal imaging libraries for correlative studies of MRI signal and histopathologic tissue findings in a model of soft-tissue sarcoma.

We have identified a preliminary collection of cytometric features that may affect MRI signatures in tumor tissues. Our observations support literature reports of possible relationships between ADC and cell density (60–62). We also discerned other cytometric features that may correlate with ADC (eg, Delaunay ratio). While ADC studies are of obvious interest, T2* studies are less commonly pursued. We chose T2* for two purposes: first, as a methodologic link to MRH based on ex vivo protocols previously established in our laboratory and second, as a functional link to future studies of oxygenation and hypoxia, including functional imaging experiments such as blood oxygen level–dependent techniques (63).

The preliminary correlations identified between in vivo MR images and histopathologic images demonstrate translational utility. Identifying differences in nuclear shape and structural variance is useful when nuclear pleomorphism is of interest to establish tumor grade, such as in cases of sarcoma (64–66). Cell packing gives rise to susceptibility-induced reduction in T2* that is enhanced at higher magnetic fields, which may account for the strong correlation observed in vivo (67). It is important to note that these measurements were made at the subtumoral scale, demonstrating the value of histologic analysis–based MRI interpretations in cases of heterogeneous tumors. Such measurements would not have been possible without the use of MRH to register disparate image types. While MRH is not performed clinically, it can be performed in preclinical models of cancer to expand our understanding of tumor MRI. These preliminary findings provide rationale for expanded tumor MRI studies and represent the first steps in translating tumor MRI features into histopathologic profiles.

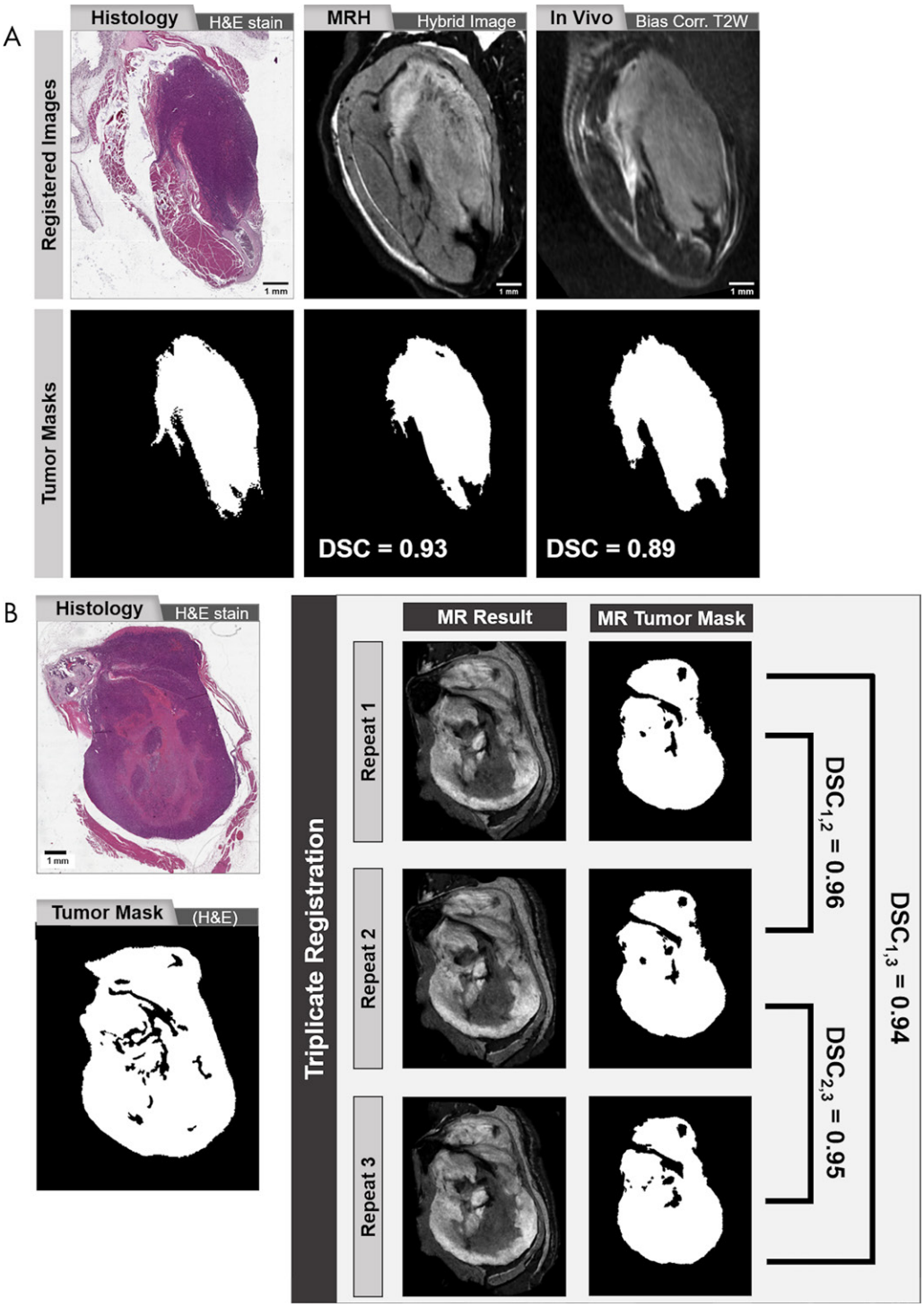

Figure 3: Assessment of image registration performed by comparing transformed tumor masks. Binary tumor masks of sample tissues are shown for comparison of multiparametric image registration to histologic images and repeated registrations. Tumor masks (black and white) were delineated on the digitized histopathologic slides, as well as on the three-dimensional (3D) ex vivo and in vivo MR images. *A*, Transformed MRI masks were compared with histopathologic masks, and Dice similarity coefficients (DSCs) were calculated to assess the registration success for in vivo and ex vivo MRI. *B*, In a subset of three samples, resulting tumor masks from triplicate registrations were compared. Corr. = correction, H&E = hematoxylin-eosin, MRH = MR histology.

As this was a pilot study, there were several limitations in the data interpretation. The first limitation was inconsistency in histopathologic sectioning, which was due in part to inadequate fixation and harsh decalcification. In subsequent works, we plan to perform perfusion fixation after imaging. A second limitation was the quality of the in vivo diffusion-weighted images, which was limited to reduce time and possible adverse effects of sustained anesthesia. The acquisition sequence has since been improved to ensure improved signal to noise in a reasonable time (<1 h). Finally, to establish protocols and

Table 2: Mean DSCs and JSCs for Assessment of Repeatability at Registration of MR Images to Histologic Images

	ex Vivo		in Vivo	
Sample	DSC	JSC	DSC	JSC
Slide 2	0.922 ± 0.005	85.6% ± 0.8	0.914 ± 0.008	84.1% ± 1.4
Slide 8	0.976 ± 0.003	95.2% ± 0.4	0.946 ± 0.001	89.3% ± 0.3
Slide 12	0.952 ± 0.006	90.9% ± 1.1	0.924 ± 0.007	85.8% ± 1.3

Note.—Data are mean Dice similarity coefficients (DSC) and Jaccard similarity coefficients (JSC) ± standard deviations for registration of ex vivo and in vivo MR images to histopathologic images. Analysis of each slide was performed in triplicate.

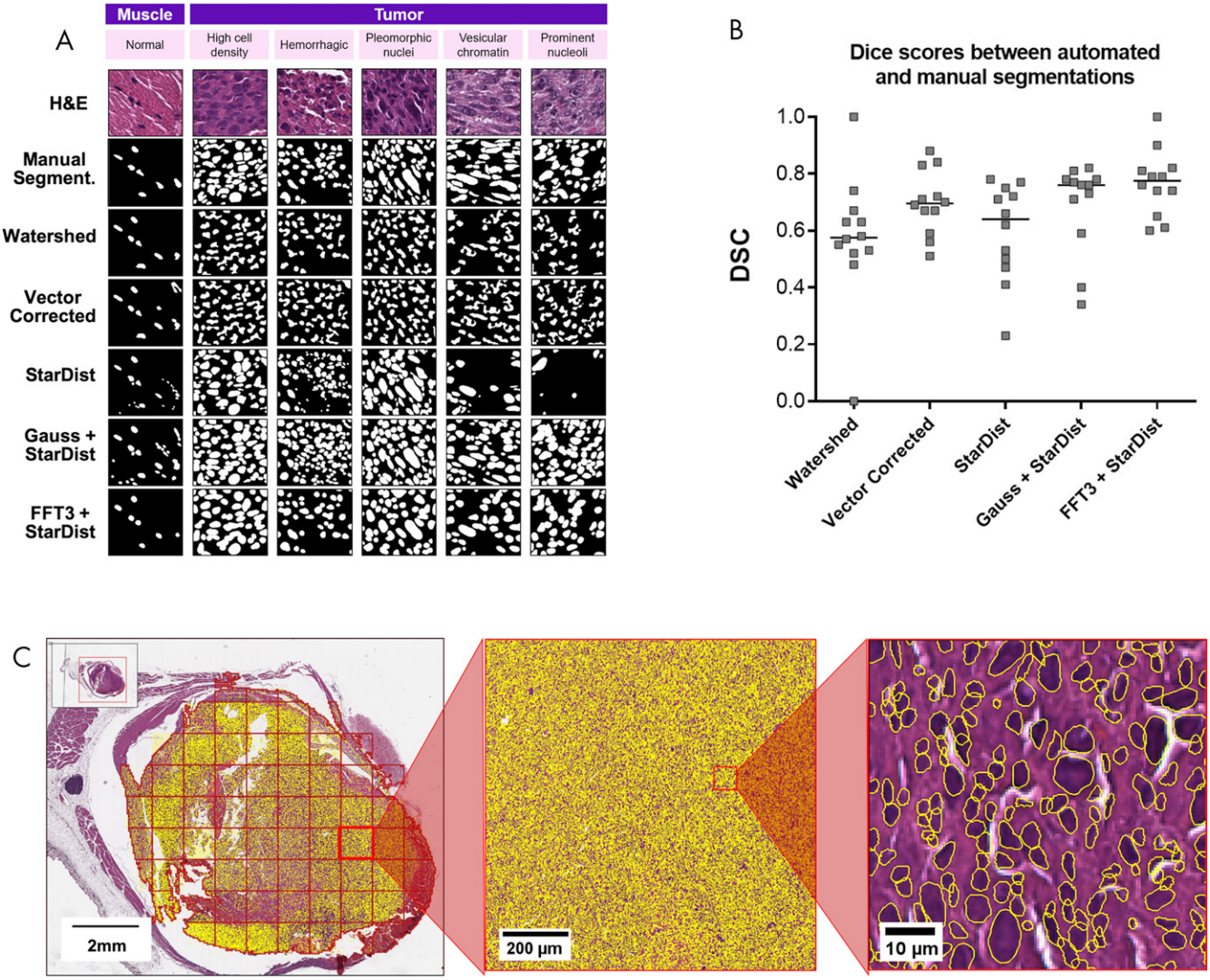

Figure 4: Refinement of automated nuclear segmentation for whole hematoxylin-eosin (H&E)–stained slides. *A*, Selected automated nuclear segmentation techniques are shown for comparison with manual segmentation in a variety of nuclear conditions present in the data set. *B*, Automated segmentation techniques were compared with manual segmentation by using Dice similarity coefficients (DSC). *C*, A sample of whole-slide nuclear segmentation is shown for a cross-section of a sarcoma-bearing hind limb. FFT3 = Fourier transform 3, Gauss = Gaussian, segment. = segmentation, StarDist = StarDist FIJI plugin for shape detection with star-convex shape priors.

demonstrate feasibility, the statistical interpretation of the preliminary data was limited to simple linear regressions within individual samples. While these findings inform the design of larger-scale studies, more sophisticated analytic approaches must be used to understand the nuanced relationships between MRI findings and tumor cytoarchitecture.

The most notable achievement of this work was that of demonstrating the capacity for statistically viable experimentation

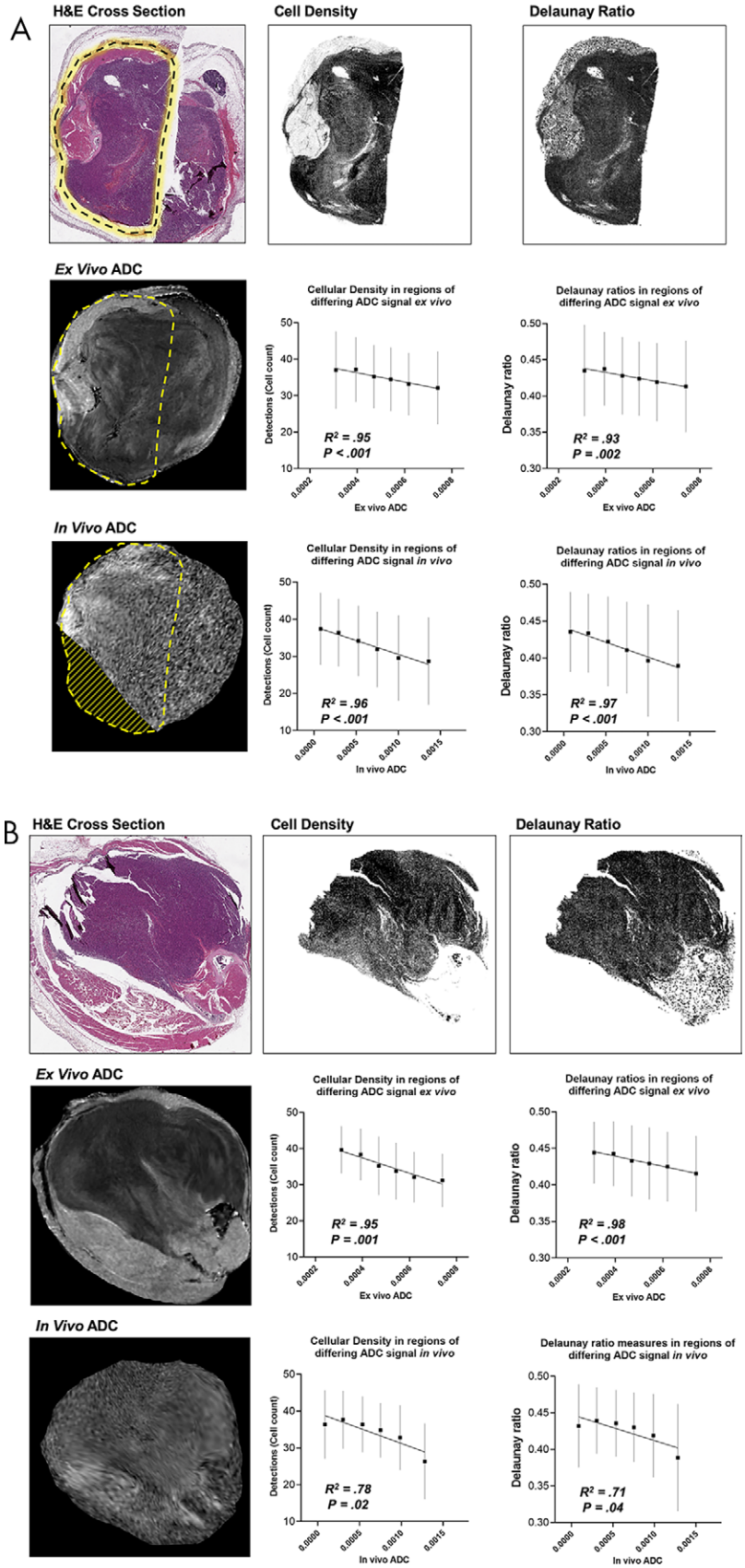

Figure 5: Relationships between ex vivo and in vivo apparent diffusion coefficients (ADC) and cytometric features of individual tissue sections. *A, B,* Shown are two examples of independent tumor samples in which ex vivo and in vivo ADC images were compared with cytometric property maps. Linear relationships were demonstrated between ADC (ex vivo and in vivo) and both cell density (middle column), and Delaunay ratio (right column). Yellow dashed lines indicate regions on the MR image that correspond to the evaluable histologic area; yellow stripes indicate regions outside of the MRI field of view. R^2 values for all linear regressions, as well as the *P* values describing the deviation of the slope from zero, are provided. H&E = hematoxylin-eosin.

with very large data sets in the Image Space environment. While the tools we used can be run on standard laboratory desktops, the size of the data limits the user to per-sample study. Image Space exhibits high-throughput capacity, facilitating robust parameter testing during pipeline assembly. The described workflow revealed significant results at subtumor spatial resolution in data sets that were formerly size prohibitive. By lifting data size restrictions, we can harness data science applications to improve and standardize the pipeline. Image registration is arguably the most cumbersome step in the pipeline. We derived a method based on tumor segmentations to assess registration accuracy and repeatability in tumor images. We found that current automatic techniques failed to align 3D MR images to 2D histopathologic images owing to discrepancies in signal type and dimensionality. With adequately powered data sets that include ex vivo MRH, we can implement machine learning and artificial intelligence techniques to automate registration. Defining automated means of performing histopathologic image and MR image registration has clear translational appeal for clinical implementation. Similar techniques can be applied to histologic slide processing, expanding understanding of how tumor heterogeneity affects MR images. We are pursuing these avenues to overcome the challenges of integrating dissimilar data and to provide a means of systematically comparing MRI signal patterns with reference-standard histopathologic tissue findings. By bridging the gap between histopathologic analysis and MRI, methodologies for noninvasive assessment of tumor architecture and microenvironments can be further investigated for implementation into clinical practice.

Acknowledgments: All small-animal imaging work was performed at the Duke Center for In Vivo Microscopy. The authors thank Yan Ma for her assistance in tissue preparation and staining, Tyler Jacks (Massachusetts Institute of Technology) for providing the *LSL-Kras*^{G12D} mice, and Anton Berns (Netherlands Cancer Institute) for providing the *p53*^{flflf} mice.

Author contributions: Guarantors of integrity of entire study, S.J.B., Y.M.M., C.T.B., G.A.J.; study concepts/study design or data acquisition or data analysis/interpretation, all authors; manuscript drafting or manuscript revision for important intellectual content, all authors; approval of final version of submitted manuscript, all authors; agrees to ensure any questions related to the work are appropriately resolved, all authors; literature research, S.J.B., G.A.J.; experimental studies, S.J.B.,

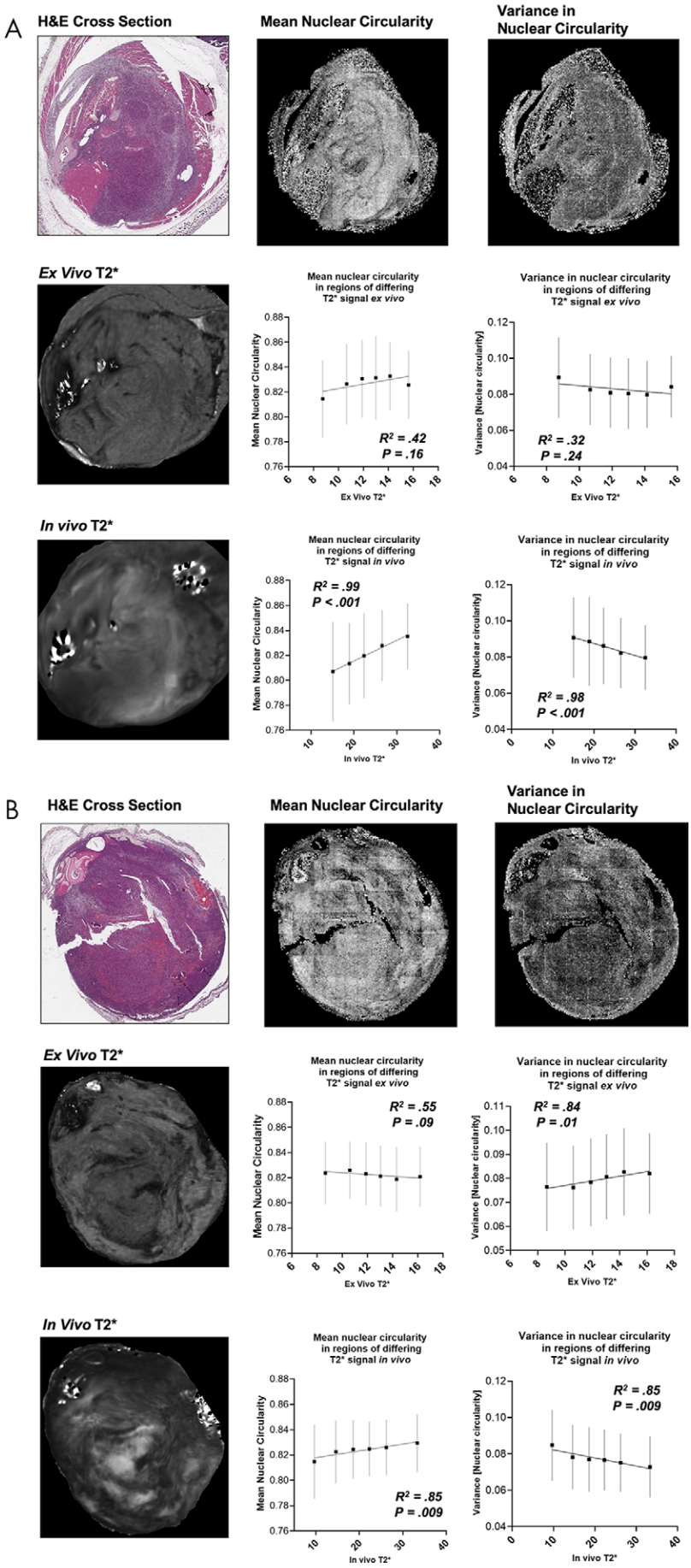

Figure 6: Relationships between ex vivo and in vivo T2* and cytometric features of individual tissue sections. *A, B,* Shown are two examples of independent tumor samples in which ex vivo and in vivo T2* images were compared with cytometric property maps. Linear relationships were demonstrated between in vivo T2* and both nuclear circularity (middle column) and variance in nuclear circularity (right column). R^2 values for all linear regressions, as well as the *P* values describing the deviation of the slope from zero, are provided. H&E = hematoxylin-eosin.

Y.M.M., J.I.E., Y.Q., G.P.C., F.Z., A.M.B., D.G.K., G.A.J.; statistical analysis, S.J.B., K.H., F.Z.; and manuscript editing, S.J.B., Y.M.M., J.I.E., F.Z., C.T.B., G.A.J.

Disclosures of Conflicts of Interest: **S.J.B.** disclosed no relevant relationships. **J.C.** disclosed no relevant relationships. **Y.M.M.** Activities related to the present article: disclosed no relevant relationships. Activities not related to the present article: institution received funds for Damon Runyon Clinical Investigator Award (K08-DE029887-01) from National Institutes of Health/NIDC, SU2C Merck Catalyst Research Grant (R44-CA224840-02) from National Institutes of Health/National Cancer Institute, and Conquer Cancer Foundation of ASCO Young Investigator Award; received payment for two educational lectures from Oakstone; paid contributor to UpToDate. Other relationships: disclosed no relevant relationships. **J.I.E.** disclosed no relevant relationships. **Y.Q.** disclosed no relevant relationships. **K.J.H.** disclosed no relevant relationships. **G.P.C.** disclosed no relevant relationships. **F.Z.** disclosed no relevant relationships. **A.M.B.** disclosed no relevant relationships. **C.T.B.** disclosed no relevant relationships. **D.G.K.** Activities related to the present article: disclosed no relevant relationships. Activities not related to the present article: member of Scientific Advisory Board of Lumicell; institution grants from Varian Medical Systems, Bristol-Meyers Squibb, and Eli Lilly; support for clinical trial of Merck Reagents from Merck, Bristol-Meyers Squibb, Calithera, and Amgen; patents from Lumicell and XRad Therapeutics; receives royalties from Lumicell and UptoDate; owns stock in XRad Therapeutics and has stock options in Lumicell. Other relationships: disclosed no relevant relationships. **G.A.J.** disclosed no relevant relationships.

References

1. Chang PD, Malone HR, Bowden SG, et al. A Multiparametric Model for Mapping Cellularity in Glioblastoma Using Radiographically Localized Biopsies. AJNR Am J Neuroradiol 2017;38(5):890–898.
2. Stamatelos SK, Bhargava A, Kim E, Popel AS, Pathak AP. Tumor Ensemble-Based Modeling and Visualization of Emergent Angiogenic Heterogeneity in Breast Cancer. Sci Rep 2019;9(1):5276.
3. Wu LM, Zhao ZZ, Chen XX, et al. Comparison of T2(*) mapping with diffusion-weighted imaging in the characterization of low-grade vs intermediate-grade and high-grade prostate cancer. Br J Radiol 2016;89(1063):20151076.
4. Ashton E, Riek J. Advanced MR techniques in multicenter clinical trials. J Magn Reson Imaging 2013;37(4):761–769.
5. El Beltagi AH, Elsotouhy AH, Own AM, Abdelfattah W, Nair K, Vattoth S. Functional magnetic resonance imaging of head and neck cancer: Performance and potential. Neuroradiol J 2019;32(1):36–52.
6. Elsherif S, Odisio EGLC, Faria S, et al. Imaging and staging of neuroendocrine cervical cancer. Abdom Radiol (NY) 2018;43(12):3468–3478.
7. Manetta R, Palumbo P, Gianneramo C, et al. Correlation between ADC values and Gleason score in evaluation of prostate cancer: multicentre experience and review of the literature. Gland Surg 2019;8(Suppl 3):S216–S222.
8. Pham TT, Liney GP, Wong K, Barton MB. Functional MRI for quantitative treatment response prediction in locally advanced rectal cancer. Br J Radiol 2017;90(1072):20151078.
9. Nasu K, Kuroki Y, Tsukamoto T, Nakajima H, Mori K, Minami M. Diffusion-weighted imaging of surgically resected hepatocellular carcinoma: imaging characteristics and relationship among signal intensity, apparent diffusion coefficient, and histopathologic grade. AJR Am J Roentgenol 2009;193(2):438–444.
10. Park IK, Yu JS, Cho ES, Kim JH, Chung JJ. Apparent diffusion coefficient of hepatocellular carcinoma on diffusion-weighted imaging: Histopathologic tumor grade versus arterial vascularity during dynamic magnetic resonance imaging. PLoS One 2018;13(5):e0197070.
11. Surov A, Chang YW, Li L, et al. Apparent diffusion coefficient cannot predict molecular subtype and lymph node metastases in invasive breast cancer: a multicenter analysis. BMC Cancer 2019;19(1):1043.
12. Roodakker KR, Alhuseinalkhudhur A, Al-Jaff M, et al. Region-by-region analysis of PET, MRI, and histology in en bloc-resected oligodendrogliomas reveals intra-tumoral heterogeneity. Eur J Nucl Med Mol Imaging 2019;46(3):569–579.
13. Han L, Wang S, Miao Y, et al. MRI texture analysis based on 3D tumor measurement reflects the IDH1 mutations in gliomas - A preliminary study. Eur J Radiol 2019;112:169–179.
14. Giammarile F, Cinotti LE, Jouvet A, et al. High and low grade oligodendrogliomas (ODG): correlation of amino-acid and glucose uptakes using PET and histological classifications. J Neurooncol 2004;68(3):263–274.
15. Inoue A, Yamaguchi K, Kurata Y, et al. Unenhanced region on magnetic resonance imaging represents tumor progression in uterine carcinosarcoma. J Gynecol Oncol 2017;28(5):e62.
16. Meyer C, Ma B, Kunju LP, Davenport M, Piert M. Challenges in accurate registration of 3-D medical imaging and histopathology in primary prostate cancer. Eur J Nucl Med Mol Imaging 2013;40(Suppl 1):S72–S78.
17. McGrath DM, Lee J, Foltz WD, et al. Technical Note: Method to correlate whole-specimen histopathology of radical prostatectomy with diagnostic MR imaging. Med Phys 2016;43(3):1065–1072.
18. Gibson E, Gaed M, Gómez JA, et al. 3D prostate histology image reconstruction: Quantifying the impact of tissue deformation and histology section location. J Pathol Inform 2013;4(1):31.
19. Iglesias JE, Van Leemput K, Golland P, Yendiki A. Joint inference on structural and diffusion MRI for sequence-adaptive Bayesian segmentation of thalamic nuclei with probabilistic atlases. Inf Process Med Imaging 2019;11492:767–779.
20. Dinis Fernandes C, Ghobadi G, van der Poel HG, et al. Quantitative 3-T multi-parametric MRI and step-section pathology of recurrent prostate cancer patients after radiation therapy. Eur Radiol 2019;29(8):4160–4168.
21. Malone SC, Haridass A, Nyiri B, et al. Creation of 3-dimensional prostate cancer maps: methodology and clinical and research implications. Arch Pathol Lab Med 2014;138(6):803–808.
22. Tan N, Margolis DJ, Lu DY, et al. Characteristics of Detected and Missed Prostate Cancer Foci on 3-T Multiparametric MRI Using an Endorectal Coil Correlated With Whole-Mount Thin-Section Histopathology. AJR Am J Roentgenol 2015;205(1):W87–W92.
23. Harmon SA, Brown GT, Sanford T, et al. Spatial density and diversity of architectural histology in prostate cancer: influence on diffusion weighted magnetic resonance imaging. Quant Imaging Med Surg 2020;10(2):326–339.
24. Glazer DI, Hassanzadeh E, Fedorov A, et al. Diffusion-weighted endorectal MR imaging at 3T for prostate cancer: correlation with tumor cell density and percentage Gleason pattern on whole mount pathology. Abdom Radiol (NY) 2017;42(3):918–925.
25. Hurrell SL, McGarry SD, Kaczmarowski A, et al. Optimized b-value selection for the discrimination of prostate cancer grades, including the cribriform pattern, using diffusion weighted imaging. J Med Imaging (Bellingham) 2018;5(1):011004.
26. Montelius M, Jalnefjord O, Spetz J, Nilsson O, Forssell-Aronsson E, Ljungberg M. Multiparametric MR for non-invasive evaluation of tumour tissue histological characteristics after radionuclide therapy. NMR Biomed 2019;32(3):e4060.
27. Al-Mubarak H, Vallatos A, Gallagher L, et al. Stacked in-plane histology for quantitative validation of non-invasive imaging biomarkers: Application to an infiltrative brain tumour model. J Neurosci Methods 2019;326:108372.
28. Vallatos A, Al-Mubarak HFI, Birch JL, et al. Quantitative histopathologic assessment of perfusion MRI as a marker of glioblastoma cell infiltration in and beyond the peritumoral edema region. J Magn Reson Imaging 2019;50(2):529–540.
29. Johnson GA, Benveniste H, Black RD, Hedlund LW, Maronpot RR, Smith BR. Histology by magnetic resonance microscopy. Magn Reson Q 1993;9(1):1–30.
30. Sitek KR, Gulban OF, Calabrese E, et al. Mapping the human subcortical auditory system using histology, postmortem MRI and in vivo MRI at 7T. eLife 2019;8:e48932.
31. Lee CL, Mowery YM, Daniel AR, et al. Mutational landscape in genetically engineered, carcinogen-induced, and radiation-induced mouse sarcoma. JCI Insight 2019;4(13):e128698.
32. Kirsch DG, Dinulescu DM, Miller JB, et al. A spatially and temporally restricted mouse model of soft tissue sarcoma. Nat Med 2007;13(8):992–997.
33. Fite BZ, Wong A, Liu Y, et al. Magnetic resonance imaging assessment of effective ablated volume following high intensity focused ultrasound. PLoS One 2015;10(3):e0120037.
34. Vormoor B, Knizia HK, Batey MA, et al. Development of a preclinical orthotopic xenograft model of Ewing sarcoma and other human malignant bone disease using advanced in vivo imaging. PLoS One 2014;9(1):e85128.
35. Beloueche-Babari M, Jamin Y, Arunan V, et al. Acute tumour response to the MEK1/2 inhibitor selumetinib (AZD6244, ARRY-142886) evaluated by non-invasive diffusion-weighted MRI. Br J Cancer 2013;109(6):1562–1569.
36. Allan Johnson G, Wang N, Anderson RJ, et al. Whole mouse brain connectomics. J Comp Neurol 2019;527(13):2146–2157.
37. Blasiak B, Landry J, Tyson R, et al. Molecular susceptibility weighted imaging of the glioma rim in a mouse model. J Neurosci Methods 2014;226:132–138.
38. Wang N, Anderson RJ, Badea A, et al. Whole mouse brain structural connectomics using magnetic resonance histology. Brain Struct Funct 2018;223(9):4323–4335.
39. Lustig M, Donoho DL, Santos JM, Pauly JM. Compressed Sensing MRI. IEEE Signal Process Mag 2008;25(2):72–82.
40. Bankhead P, Loughrey MB, Fernández JA, et al. QuPath: Open source software for digital pathology image analysis. Sci Rep 2017;7(1):16878.
41. Fedorov A, Beichel R, Kalpathy-Cramer J, et al. 3D Slicer as an image computing platform for the Quantitative Imaging Network. Magn Reson Imaging 2012;30(9):1323–1341.
42. Blocker SJ, Mowery YM, Holbrook MD, et al. Bridging the translational gap: Implementation of multimodal small animal imaging strategies for tumor burden assessment in a co-clinical trial. PLoS One 2019;14(4):e0207555.
43. Slicer Wiki. https://www.slicer.org/wiki/Documentation/4.4/Modules/Transforms. 2019.
44. Myronenko A, Song X. Point set registration: coherent point drift. IEEE Trans Pattern Anal Mach Intell 2010;32(12):2262–2275.
45. Slicer Wiki. https://www.slicer.org/wiki/Documentation/Nightly/Modules/LandmarkRegistration. 2018.
46. Taha AA, Hanbury A. Metrics for evaluating 3D medical image segmentation: analysis, selection, and tool. BMC Med Imaging 2015;15(1):29.
47. Zou KH, Warfield SK, Bharatha A, et al. Statistical validation of image segmentation quality based on a spatial overlap index. Acad Radiol 2004;11(2):178–189.
48. Gudla PR, Nandy K, Collins J, Meaburn KJ, Misteli T, Lockett SJ. A high-throughput system for segmenting nuclei using multiscale techniques. Cytometry A 2008;73(5):451–466.
49. Salvi M, Molinari F. Multi-tissue and multi-scale approach for nuclei segmentation in H&E stained images. Biomed Eng Online 2018;17(1):89.
50. Schneider CA, Rasband WS, Eliceiri KW. NIH Image to ImageJ: 25 years of image analysis. Nat Methods 2012;9(7):671–675.

51. Schindelin J, Arganda-Carreras I, Frise E, et al. Fiji: an open-source platform for biological-image analysis. Nat Methods 2012;9(7):676–682.
52. Schmidt U, Weigert M, Broaddus C, Myers G. Cell Detection with Star-Convex Polygons. In: Frangi A, Schnabel J, Davatzikos C, Alberola-López C, Fichtinger G, eds. Medical Image Computing and Computer Assisted Intervention – MICCAI 2018. MICCAI 2018. Lecture Notes in Computer Science, vol 11071. Cham, Switzerland: Springer, 2018; 265–273.
53. Haralick RM, Shanmugam K, Dinstein I. Textural Features for Image Classification. IEEE Trans Syst Man Cybern 1973;SMC-3(6):610–621.
54. Ren J, Sadimin ET, Wang D, Epstein JI, Foran DJ, Qi X. Computer aided analysis of prostate histopathology images Gleason grading especially for Gleason score 7. Annu Int Conf IEEE Eng Med Biol Soc 2015;2015:3013–3016.
55. He M, Kaushik SS, Robertson SH, et al. Extending semiautomatic ventilation defect analysis for hyperpolarized (129)Xe ventilation MRI. Acad Radiol 2014;21(12):1530–1541.
56. Wang Z, Robertson SH, Wang J, et al. Quantitative analysis of hyperpolarized 129 Xe gas transfer MRI. Med Phys 2017;44(6):2415–2428.
57. Cserni G, Chmielik E, Cserni B, Tot T. The new TNM-based staging of breast cancer. Virchows Arch 2018;472(5):697–703.
58. Huang SH, O'Sullivan B. Overview of the 8th Edition TNM Classification for Head and Neck Cancer. Curr Treat Options Oncol 2017;18(7):40.
59. Paner GP, Gandhi J, Choy B, Amin MB. Essential Updates in Grading, Morphotyping, Reporting, and Staging of Prostate Carcinoma for General Surgical Pathologists. Arch Pathol Lab Med 2019;143(5):550–564.
60. Chen L, Liu M, Bao J, et al. The correlation between apparent diffusion coefficient and tumor cellularity in patients: a meta-analysis. PLoS One 2013;8(11):e79008.
61. Fan G, Zang P, Jing F, Wu Z, Guo Q. Usefulness of diffusion/perfusion-weighted MRI in rat gliomas: correlation with histopathology. Acad Radiol 2005;12(5):640–651.
62. Surov A, Meyer HJ, Wienke A. Correlation Between Minimum Apparent Diffusion Coefficient (ADCmin) and Tumor Cellularity: A Meta-analysis. Anticancer Res 2017;37(7):3807–3810.
63. Tóth V, Förschler A, Hirsch NM, et al. MR-based hypoxia measures in human glioma. J Neurooncol 2013;115(2):197–207.
64. Mijovic Z, Kostov M, Mihailovic D, Zivkovic N, Stojanovic M, Zdravkovic M. Correlation of nuclear morphometry of primary melanoma of the skin with clinicopathological parameters and expression of tumor suppressor proteins (p53 and p16(INK4a)) and bcl-2 oncoprotein. J BUON 2013;18(2):471–476.
65. Schöchlin M, Weissinger SE, Brandes AR, Herrmann M, Möller P, Lennerz JK. A nuclear circularity-based classifier for diagnostic distinction of desmoplastic from spindle cell melanoma in digitized histological images. J Pathol Inform 2014;5(1):40.
66. Yang W, Tian R, Xue T. Nuclear shape descriptors by automated morphometry may distinguish aggressive variants of squamous cell carcinoma from relatively benign skin proliferative lesions: a pilot study. Tumour Biol 2015;36(8):6125–6131.
67. Johnson GA, Herfkens RJ, Brown MA. Tissue relaxation time: in vivo field dependence. Radiology 1985;156(3):805–810.